

Article

Evaluation of Chlorophyll-*a* Estimation Approaches Using Iterative Stepwise Elimination Partial Least Squares (ISE-PLS) Regression and Several Traditional Algorithms from Field Hyperspectral Measurements in the Seto Inland Sea, Japan

Zuomin Wang ¹ , Yuji Sakuno ^{1,*} , Kazuhiko Koike ² and Shizuka Ohara ² 

¹ Graduate School of Engineering, Hiroshima University, 1-4-1 Kagamiyama, Higashi-Hiroshima, Hiroshima 739-8527, Japan; wangzuomin123@gmail.com

² Graduate School of Biosphere Science, Hiroshima University, 1-4-4 Kagamiyama, Higashi-Hiroshima, Hiroshima 739-8528, Japan; kazkoike@hiroshima-u.ac.jp (K.K.); oharashizu@hiroshima-u.ac.jp (S.O.)

* Correspondence: sakuno@hiroshima-u.ac.jp; Tel.: +81-82-424-7773

Received: 1 June 2018; Accepted: 10 August 2018; Published: 13 August 2018



Abstract: Harmful algal blooms (HABs) occur frequently in the Seto Inland Sea, bringing significant economic and environmental losses for the area, which is well known as one of the world's most productive fisheries. Our objective was to develop a quantitative model using in situ hyperspectral measurements in the Seto Inland Sea to estimate chlorophyll *a* (Chl-*a*) concentration, which is a significant parameter for detecting HABs. We obtained spectra and Chl-*a* data at six stations from 12 ship-based surveys between December 2015 and September 2017. In this study, we used an iterative stepwise elimination partial least squares (ISE-PLS) regression method along with several empirical and semi-analytical methods such as ocean chlorophyll, three-band model, and two-band model algorithms to retrieve Chl-*a*. Our results showed that ISE-PLS using both the water-leaving reflectance (R_L) and the first derivative reflectance (FDR) had a better predictive ability with higher coefficient of determination (R^2), lower root mean squared error (RMSE), and higher residual predictive deviation (RPD) values ($R^2 = 0.77$, RMSE = 1.47 and RPD = 2.1 for R_L ; $R^2 = 0.78$, RMSE = 1.45 and RPD = 2.13 for FDR). However, in this study the ocean chlorophyll (OC) algorithms had poor predictive ability and the three-band and two-band model algorithms did not perform well in areas with lower Chl-*a* concentrations. These results support ISE-PLS as a potential coastal water quality assessment method using hyperspectral measurements.

Keywords: water quality; remote sensing; harmful algal bloom; partial least squares regression

1. Introduction

The Seto Inland Sea is an approximately 23,000 km² semi-enclosed coastal sea in western Japan, with an average depth of 38 m. This sea is well-known as one of the world's most productive fisheries due to its abundance of fish and variety of fish species [1]. Approximately 35 million people live around the Seto Inland Sea, bringing increased industrialization and urbanization that have made the Seto Inland Sea one of Japan's most industrialized regions [2]. However, productivity of fisheries is sensitive and thus vulnerable to anthropogenic stress. Eutrophication of coastal waters has affected fishing and other activities by contributing to harmful algal blooms (HABs), also known as red tides. HABs frequently occurred in the Seto Inland Sea during a period of high economic growth in the 1970s [3]. Although HABs have decreased from about 300 cases per year in 1976 to about 100 cases per

year more recently [4], severe damage to fisheries and significant economic losses due to HABs are still occurring [5]. Therefore, monitoring HABs is vital for managing the fisheries industry and ensuring sea water quality.

The scientific community and various agencies monitor HABs to manage and control them. Many studies have conducted HABs observation, but most have relied on conventional in situ ship surveys and buoy stations [6]. For each observation, water samples must be collected and analyzed under controlled lab environments, which is costly and time consuming. Additionally, the spatial scale of such surveys is limited. Remote sensing has been widely applied to monitor, in real time, various ocean environment factors on a large scale using spaceborne or airborne instruments. Having a high degree of spatial and temporal coverage over a large scale is convenient for monitoring HABs. Several studies have shown distributions of HABs using satellite imagery and chlorophyll *a* (Chl-*a*) concentration measurements [7,8]. Chl-*a* concentration in water is a major indicator of a trophic state and oceanic Chl-*a* concentration is the most common property characterizing first trophic levels in marine environments [9]. Chl-*a* acts as a link between nutrient concentration and algal production [10], therefore, it can be used as a proxy to evaluate HABs.

Earlier studies indicated bio-optical models were usually used to estimate Chl-*a* concentrations in water [11], which are based on the inherent optical properties (IOPs) in a water body, that is, the absorption and backscattering dominated by Chl-*a*, colored dissolved organic matter (CDOM), and suspended matters etc. Chl-*a* can be estimated when the relationship between IOPs and the remote sensing reflectance (R_{rs}) is built. Basing on the bio-optical properties, several algorithms developed to estimate Chl-*a* in the open sea and coastal area, such as the ocean chlorophyll 2-band (OC2), ocean chlorophyll 3-band (OC3), and ocean chlorophyll 4-band (OC4) algorithms used for the standard Sea-viewing Wide Field-of-view Sensor (SeaWiFS) Chl-*a* product [12,13]. The strong Chl-*a* absorption in red bands and diminishing Chl-*a* absorption and increasing water absorption in near infrared (NIR) bands [14] yields a band ratio between the NIR and red bands that has frequently been used to estimate Chl-*a* concentrations [15–17]. Han and Rundquist [18] found that the ratio of reflectance at 705 nm (NIR) to reflectance at 670 nm (red) correlated well with Chl-*a* concentration in a turbid reservoir. Additionally, a three-band semi-analytical reflectance model can be used to assess Chl-*a* concentration by taking advantage of the red and NIR regions' absorption characteristics. This model was originally developed to estimate pigment content in higher plant leaves [19].

Partial least squares (PLS) regression, a statistical method developed by Wold [20], is an efficient tool for multivariate modeling that is increasingly used to handle high-dimensional hyperspectral data [21,22]. Its potential application for water quality quantification has been tested [23], and the iterative stepwise elimination PLS (ISE-PLS) [24], which combines PLS and a wavelength selection function, has proven effective at estimating Chl-*a* in inland irrigation ponds water [25]. However, ISE-PLS has not been tested in coastal waters or compared with traditional algorithms.

Our objectives are: (1) to develop models to estimate Chl-*a* using in situ hyperspectral data; (2) to evaluate traditional empirical and semi-analytical algorithms in the Seto Inland Sea; and (3) to evaluate the ISE-PLS method's accuracy in coastal waters.

2. Materials and Methods

2.1. Study Area

The study area is in the central part of the Seto Inland Sea near the city of Fukuyama as shown in Figure 1. We selected six sites as sampling stations, which are described in Table 1. The study area has an average water depth of 17.3 m and water temperatures range from 7.3 °C (winter) to 28.4 °C (summer). The Seto Inland Sea is rich in fishery resources, with more than 50% of the total fish production contributed by aquaculture production. Additionally, there are approximately 17 fish farms being operated in the Tashima and Yokota areas near our study area [26]. Consequently, there

are a range of organic compounds released by fish farm waste that may affect eutrophication due to dissolved nitrogen [27].

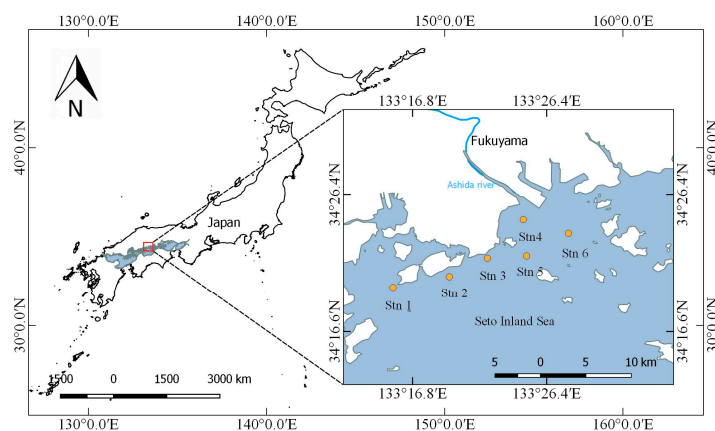


Figure 1. Research site locations in this study.

Table 1. Stations for data collection in the study.

Station ID	Latitude	Longitude	Depth (m)
1	34°19'44" N	133°15'24" E	29
2	34°20'31" N	133°19'26" E	17
3	34°21'51" N	133°22'10" E	10
4	34°24'37" N	133°24'44" E	10
5	34°22'01" N	133°24'58" E	21
6	34°23'38" N	133°27'58" E	17

2.2. Data Collection and Pre-Processing

We conducted 12 ship-based surveys between 16 December 2015, and 7 September 2017 at six stations (Figure 1). We performed in situ measurements of water-leaving reflectance (R_L) using a MS-720 (Eiko Co. Ltd., Tokyo, Japan) spectrometer, with a spectral range of 350–1050 nm and a spectral interval of 3.3 nm. We interpolated the spectral interval to 1 nm when exporting data. We gathered spectral readings approximately 1 m above the water surface, with a probe field angle of 25°, between 9:00 a.m. and 11:00 a.m. under clear sky conditions. We measured Chl-*a* using a Hydrolab DS5 (Hach, Loveland, CO, USA) multiparameter data sonde with sensors for measuring Chl-*a* (range from 0 to 500 µg/L) and other water quality parameters (e.g., temperature, salinity, dissolved oxygen, etc.). In this study we used Chl-*a* data from just beneath the water surface.

With respect to spectral data, we identified reflectance ranges of 325–399 nm and 901–1075 nm as noise and removed them. We then smoothed the spectral data using a Savitzky-Golay filter with 15 smoothing points. To compare the performance for Chl-*a* estimation with the original water-leaving reflectance, we also computed the first derivative reflectance (FDR), which is calculated as the difference of water-leaving reflectance for two adjacent wavebands.

2.3. OC Algorithms

In this study we used the newest ocean chlorophyll (OC) algorithms (version 6) [28], which was formulated as a fourth-order polynomial with five coefficients. The newest OC algorithms yielded better statistical agreement between model data and Chl-*a* than the first version OC algorithm [12], which was a modified cubic polynomial relationship between Chl-*a* and a ratio of remote sensing reflectance R_{rs} .

Remote sensing reflectance $R_{rs}(\lambda)$ can be represented by the relationship with water-leaving reflectance $R_L(\lambda)$ as follows [29]:

$$R_{rs}(\lambda) = \pi R_L(\lambda) \quad (1)$$

where λ is wavelength. The version 6 OC algorithms use a fourth-order polynomial equation that can be written as:

$$\log_{10}(\text{Chl}_a) = a_0 + a_1R + a_2R^2 + a_3R^3 + a_4R^4 \quad (2)$$

where $R = \log_{10}(R_{rs}(\lambda_1)/R_{rs}(\lambda_2))$ and the coefficients $a_0, a_1, a_2, a_3,$ and a_4 are different in the OC2, OC3, and OC4 algorithms. OC2 uses the blue/green ratio $R_{rs}(\text{blue})/R_{rs}(\text{green})$ and R is described as $R = \log_{10}(\frac{R_{rs}(\text{blue})}{R_{rs}(\text{green})})$. OC3 uses a three-band formulation with a maximum of R_{rs} band ratios $R_{rs}(\text{blue1})/R_{rs}(\text{green})$ and $R_{rs}(\text{blue2})/R_{rs}(\text{green})$, and R is expressed as $R = \log_{10}(\frac{R_{rs}(\text{blue1}) > R_{rs}(\text{blue2})}{R_{rs}(\text{green})})$. Similarly, OC4 uses the maximum of three R_{rs} ratios $R_{rs}(\text{blue1})/R_{rs}(\text{green})$, $R_{rs}(\text{blue2})/R_{rs}(\text{green})$ and $R_{rs}(\text{blue3})/R_{rs}(\text{green})$ —to build the formulation, with R expressed as $R = \log_{10}(\frac{R_{rs}(\text{blue1}) > R_{rs}(\text{blue2}) > R_{rs}(\text{blue3})}{R_{rs}(\text{green})})$. The OC4 algorithm has been considered a standard method for satellite detection of HABs over global waters [30,31].

In view of the sensor differences between the hyperspectral spectrometer used for in situ measurements and the SeaWiFS satellite sensor, we recalculated the parameters for Equation (2) by model recalibration using in situ Chl-*a* and R_{rs} , which was in accordance with specified OC algorithm wavebands.

2.4. Three-Band Model

The three-band model uses the NIR and red wavebands and is formulated as [19,32]:

$$\text{Chl} - a \propto (R_{\lambda_1}^{-1} - R_{\lambda_2}^{-1}) \times R_{\lambda_3} \quad (3)$$

where R_{λ_i} is the reflectance at a wavelength of λ_i nm. Previous study found the optimal spectral ranges for these wavelengths to be, $\lambda_1 = 660\text{--}670$ nm, which is maximally sensitive to absorption by Chl-*a*; $\lambda_2 = 690\text{--}720$ nm, which is minimally sensitive to absorption by Chl-*a*; and $\lambda_3 = 720\text{--}750$ nm, which is minimally affected by absorption by any constituents (e.g., Chl-*a*, suspended solids, etc.) [32,33]. We expected to find the optimal spectral ranges of $\lambda_1, \lambda_2,$ and λ_3 for Chl-*a* estimation by spectrally tuning the conceptual model using a stepwise technique [34]. First, we set λ_2 and λ_3 to 700 nm and 750 nm, respectively, and then linearly regressed using all available bands and Chl-*a* to obtain the first estimate of λ_1 , with which there was a high correlation coefficient (r). After we fixed λ_1 , we set λ_2 as an unknown waveband and linearly regressed to find an optimal λ_2 based on the best r value using the reflectance corresponding to a fixed λ_1 and an assumed λ_3 . Analogously, we confirmed the optimal λ_3 using the reflectance corresponding with fixed λ_1 and λ_2 values.

2.5. Two-Band Model

The NIR/red two-band model has been widely used to retrieve Chl-*a* concentrations in turbid productive waters to identify phytoplankton blooms [35]. This model is formulated as follows:

$$\text{Chl} - a \propto R_{\lambda_1}^{-1} \times R_{\lambda_2} \quad (4)$$

where λ_1 is in the red region and λ_2 is in NIR region. According to the band tuning method [34], we tuned the model to select the optimal NIR and red bands for Chl-*a* retrieval in this research area and compared its accuracy with the previous model, i.e., NIR/red model using wavelengths of 705 nm in the NIR region and 670 nm in the red region [18].

2.6. ISE-PLS

Partial least square (PLS) is useful for handling many descriptors even when co-linearity and noise in the model building regression are present [36]. The standard PLS regression equation can be expressed as follows:

$$y = \beta_1 x_1 + \beta_2 x_2 + \dots + \beta_i x_i + \varepsilon \quad (5)$$

where y is the response variable that represents Chl- a , x_i is the predictor variable representing spectral data such as R_L or FDR values for spectral bands 1 to i (400–900 nm), β_i is the estimated weighted regression coefficient, and ε is the error vector. In the PLS model, the original predictor variables (x) are projected onto a small number of orthogonal latent variables to simplify their relationships with response variables (y) [37]. We selected the optimal number of latent variables (NLV) in the final model using the leave-one-out (LOO) cross-validation method with a minimum value of the root mean squared error (RMSE), which is calculated as follows:

$$\text{RMSE} = \sqrt{\frac{\sum_{i=1}^n (y_i - y_p)^2}{n}} \quad (6)$$

where y_i and y_p represent sample i 's measured and predicted Chl- a , respectively, and n is the number of samples in the dataset ($n = 59$).

The iterative stepwise elimination PLS (ISE-PLS) uses a model-wise elimination technique [24] that permits the removal of less useful descriptors to improve predictive performance. This process is based on the importance of the predictor z_i , which is defined as:

$$z_i = \frac{|\beta_i|s_i}{\sum_{i=1}^I |\beta_i|s_i} \quad (7)$$

where I is the maximum number of variables, s_i is the standard deviation of predictor x_i (each predictor includes 59 samples). PLS modeling uses all available wavebands (501 bands between 400 and 900 nm). Predictors are then evaluated based on the value of the importance of predictor z_i . The predictor with minimum importance (i.e., the minimum z_i) is eliminated in each elimination cycle and the remaining predictors are used to recalibrate the model [38]. Finally, a model with maximum predictive ability is selected using the minimum RMSE value from the cross-validation.

2.7. Evaluation of Predictive Ability

We used the coefficient of determination (R^2), RMSE, and bias to evaluate the predictive ability of empirical and semi-analytical algorithms such as OC, three-band, and two-band model algorithms. Higher R^2 values and a lower RMSE indicate better Chl- a estimation performance, and bias represents systematic difference between actual and predicted values. To evaluate the ISE-PLS predictive ability, we used R^2 and RMSE from the LOO cross-validation in the final model. Additionally, we introduced the residual predictive deviation (RPD), which is defined as the ratio of the standard error of the prediction to the standard deviation, as the evaluating indicator. RPD can be expressed as $\text{RPD} = \text{SD}/\text{RMSE}$ [39]. As shown in a previous study by Chang and Laird (2002) [40], an $\text{RPD} > 2$ indicates a model with good predictive ability, $1.4 < \text{RPD} < 2$ indicates moderately good model in need of some improvement, and an $\text{RPD} < 1.4$ means the model has poor predictive ability. Finally, a method for NLV selection was used in the final PLS model, which has been reported can lower the risk of over-fitting [41]. The evaluation was basing on the sum of RMSE in cross-validation and Jaggedness (J), defined as:

$$J_j = \sum_{i=2}^I \sqrt{(\beta_{ji} - \beta_{ji-1})^2} \quad (8)$$

where j is NLV and β_{ji} represents the regression coefficient when using j latent variables. At first, the RMSE in cross-validation and J were calculated from each NLV model (maximum of 10 latent

variables were set) basing on ISE-PLS selected variables, then each value was rescaled to the range [0–1] as follows:

$$\text{RMSE}_r = \frac{\text{RMSE} - \text{RMSE}_{\min}}{\text{RMSE}_{\max} - \text{RMSE}_{\min}} \quad (9)$$

$$J_r = \frac{J - J_{\min}}{J_{\max} - J_{\min}} \quad (10)$$

where the subscript *r* refers to rescaled. The lowest value of $\text{RMSE}_r + J_r$ indicates the optimal NLV for the final PLS model.

We performed all data handling and regression analyses using Matlab software version 8.6 (MathWorks, Sherborn, MA, USA).

3. Results

3.1. Chl-*a* Characteristics and Spectral Data

Table 2 shows Chl-*a* concentration descriptive statistics from this study, including stations, number of samples, minimum (Min), maximum (Max), mean, standard deviation (SD) and coefficient of variation (CV).

Table 2. Chl-*a* concentration (µg/L) descriptive statistics.

Stations	<i>N</i>	Min	Max	Mean	SD	CV
1	12	0.83	4.2	2.73	0.95	0.35
2	12	1.06	6.72	3.82	2.15	0.56
3	12	1.72	7.84	4.5	1.71	0.38
4	12	2.31	14.33	8.13	4.54	0.56
5	6	1.75	5.46	3.92	1.25	0.32
6	5	1.2	8.74	4.41	2.84	0.64
Total	59	0.83	14.33	4.67	3.11	0.67

N, number of samples; SD, standard deviation; CV, coefficient of variation.

3.2. Comparison of Empirical and Semi-Analytical Models

3.2.1. Performance of Models for All Dataset

We used several empirical and semi-analytical models for Chl-*a* retrieval, the results of which are shown in Table 3. We initially used three standard empirical algorithms, OC2, OC3, and OC4. The first row of Figure 2 shows scatter plots between in situ measured Chl-*a* and Chl-*a* derived from OC models. The results show a linear relationship between measured and modelled Chl-*a* for all three OC algorithms, with poor R^2 values (0.36, 0.31, and 0.30, respectively for OC2, OC3, and OC4). In addition, results of all three OC algorithms underestimate Chl-*a*, indicated by the bias (−2.32, −2.71, and −2.70, respectively for OC2, OC3, and OC4). The second row of Figure 2 shows scatter plots between recalibrated OC algorithms and Chl-*a*. The R^2 values for all three OC algorithms were slightly improved (0.39, 0.36, and 0.35 respectively for OC2, OC3, and OC4), and scattered points were closer to the 1:1 line with a smaller bias (−0.46, −0.49, and −0.49, respectively for OC2, OC3, and OC4). For both the standard and recalibrated OC models, the OC2 algorithm performed better than OC3 and OC4 for Chl-*a* retrieval in this study; however, its predictive ability remains poor due to its low R^2 value.

The three-band and two-band algorithms were both based on the NIR region, which has high absorption by water, and the red region, which has high absorption by Chl-*a*. Figure 3 shows the three-band algorithm tuning process. The optimal λ_1 appeared at 664 nm where the *r* value is highest when using assumed λ_2 and λ_3 values of 700 nm and 750 nm, respectively. λ_2 and λ_3 appeared at 695 nm and 736 nm when using the tuning method. These results showed a linear relationship between the three-band algorithm and Chl-*a* concentration with a R^2 value of 0.46, as shown in Figure 4.

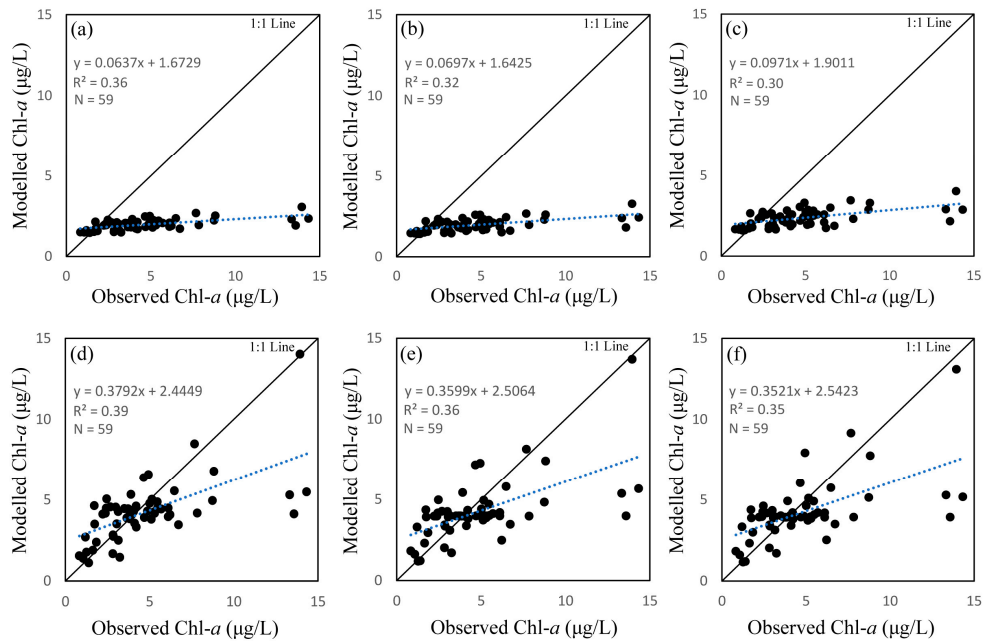


Figure 2. Correlation between observed and modelled chlorophyll *a* (Chl-*a*) using ocean chlorophyll (OC) algorithms. The first row shows results using standard coefficients (a) OC2; (b) OC3; and (c) OC4. The second row shows results from recalibrated OC models using the dataset of this study (d) OC2; (e) OC3; and (f) (OC4).

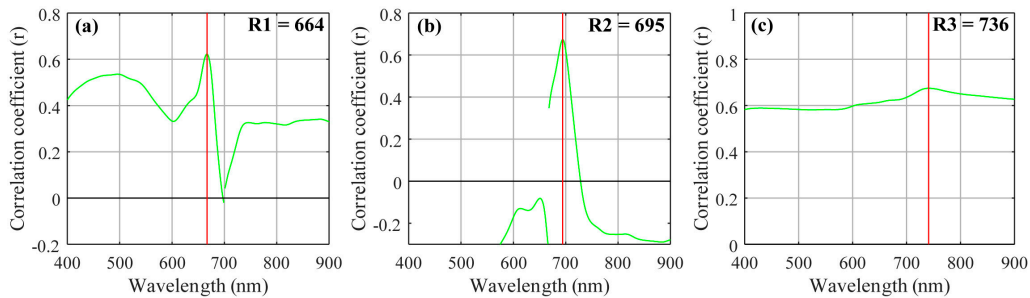


Figure 3. Selected wavebands for the three-band model algorithm using the tuning method (a) optimal band λ1; (b) optimal band λ2; and (c) optimal band λ3.

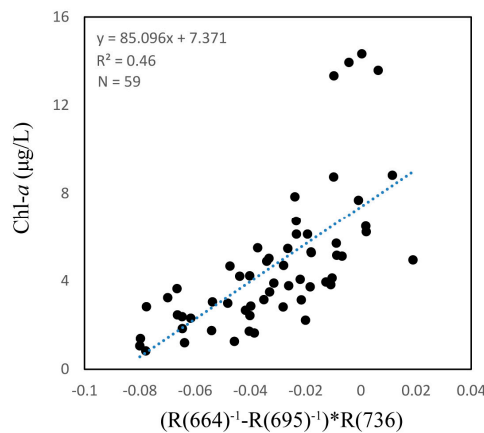


Figure 4. Correlation between the three-band model algorithm and measured chlorophyll *a* (Chl-*a*).

Table 3. Regression models used to estimate Chl-*a* concentrations.

Algorithms	Results Equation	Bands Combination (R), Coefficient <i>a</i> , and Intercept <i>b</i>	R ²	RMSE	Bias
OC2	$\text{Chl}_a = 10^{a_0+a_1R+a_2R^2+a_3R^3+a_4R^4}$	$R = \log_{10} \left(\frac{R_{rs}(490)}{R_{rs}(555)} \right)$ $a = [0.2511 \ -2.0853 \ 1.5035 \ -3.1747 \ 0.3383]$	0.36	3.96	-2.32
OC3	$\text{Chl}_a = 10^{a_0+a_1R+a_2R^2+a_3R^3+a_4R^4}$	$R = \log_{10} \left(\frac{R_{rs}(443) > R_{rs}(490)}{R_{rs}(555)} \right)$ $a = [0.2515 \ -2.3798 \ 1.5823 \ -0.6372 \ -0.5692]$	0.32	3.95	-2.71
OC4	$\text{Chl}_a = 10^{a_0+a_1R+a_2R^2+a_3R^3+a_4R^4}$	$R = \log_{10} \left(\frac{R_{rs}(443) > R_{rs}(490) > R_{rs}(510)}{R_{rs}(555)} \right)$ $a = [0.3272 \ -2.9940 \ 2.7218 \ -1.2259 \ -0.5683]$	0.30	3.66	-2.70
Recalibrated OC2	$\text{Chl}_a = 10^{a_0+a_1R+a_2R^2+a_3R^3+a_4R^4}$	$R = \log_{10} \left(\frac{R_{rs}(490)}{R_{rs}(555)} \right)$ $a = [-8942.6 \ -2053.3 \ -100.25 \ -3.8257 \ 0.5738]$	0.39	2.65	-0.46
Recalibrated OC3	$\text{Chl}_a = 10^{a_0+a_1R+a_2R^2+a_3R^3+a_4R^4}$	$R = \log_{10} \left(\frac{R_{rs}(443) > R_{rs}(490)}{R_{rs}(555)} \right)$ $a = [5204.7 \ -461.22 \ -41.033 \ -4.4207 \ 0.5491]$	0.36	2.50	-0.49
Recalibrated OC4	$\text{Chl}_a = 10^{a_0+a_1R+a_2R^2+a_3R^3+a_4R^4}$	$R = \log_{10} \left(\frac{R_{rs}(443) > R_{rs}(490) > R_{rs}(510)}{R_{rs}(555)} \right)$ $a = [-30610 \ -4098 \ -57.405 \ -0.1942 \ 0.5933]$	0.35	2.53	-0.49
Three-band	$\text{Chl}_a = aR + b$	$R = (R(664))^{-1} - R(695))^{-1} \times R(736)$ $a = 85.096 \ b = 7.371$	0.46	2.28	3.2×10^{-6}
NIR/red	$\text{Chl}_a = aR + b$	$R = R(705) \times R(670)^{-1}$ $a = 0.0044 \ b = 0.8863$	0.17	4.88	1.8×10^{-4}
NIR/red tuning	$\text{Chl}_a = aR + b$	$R = R(693) \times R(666)^{-1}$ $a = 66.633 \ b = -59.755$	0.39	2.40	2.9×10^{-6}

OC2, ocean chlorophyll-2; OC3, ocean chlorophyll-3; OC4, ocean chlorophyll-4; NIR, near-infrared.

The two-band NIR red model results showed an incompact linear relationship between the reflectance ratios of 705 nm and 670 nm and measured Chl-*a*, with a poor R² value of 0.17, as shown in Figure 5a. As with the three-band model, we tuned the spectral position to obtain the optimal NIR and red wavebands. We initially set the NIR waveband to 705 nm and then selected the optimal red region waveband, which we set from 620 nm to 680 nm based on the highest *r* value. Figure 6a shows that 666 nm was the optimal red waveband with a *r* value of 0.43. After fixing the optimal red waveband, we selected the optimal NIR region waveband, which we set from 680 nm to 740 nm. As shown in Figure 6b, we selected 693 nm as the best NIR waveband with a *r* value of 0.63. Figure 5b shows a linear relationship between the reflectance ratios of 693 nm and 666 nm and measured Chl-*a*, with a R² of 0.39.

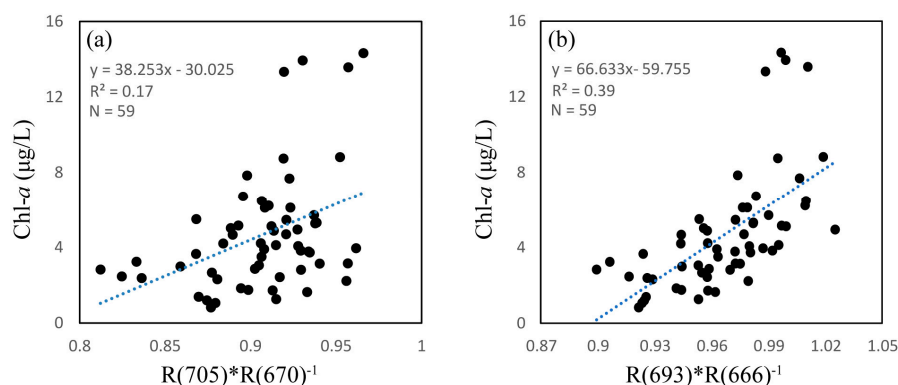


Figure 5. Relationship between observed chlorophyll *a* (Chl-*a*) concentration and near-infrared/red reflectance ratio, (a) Ratio of R(705) to R(670); (b) Ratio of R(693) to R(666).

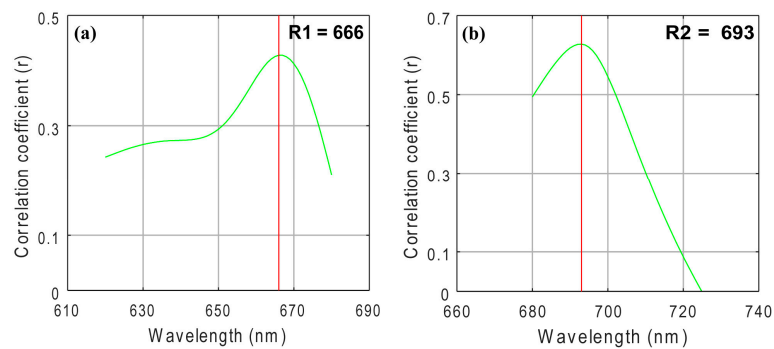


Figure 6. Selected wavebands for near-infrared/red algorithm using the tuning method (a) optimal band λ_1 ; (b) optimal band λ_2 .

3.2.2. Performance of Models for Separated Dataset

Remote sensing methods for retrieving water quality parameters contain spatial and temporal variations because the water body components that affect reflection properties vary in space and time. To further clarify the most fitted Chl-*a* retrieval method in the research area, we analysed algorithms using a separated dataset of six stations. Figure 7 shows the R_L and average R_L of each station for the research period. As we can see, the average R_L of each station shows little difference those of the others. Especially at station 4 (Figure 7d), there is an obvious reflectance peak around 580 nm, which is a result of minimum absorption by all pigments [42]. Figure 1 shows that station 4 is near a river, which could bring various nutrients from land to the coastal area. Consequently, the highest max Chl-*a* and SD values were obtained at station 4, as shown in Table 2.

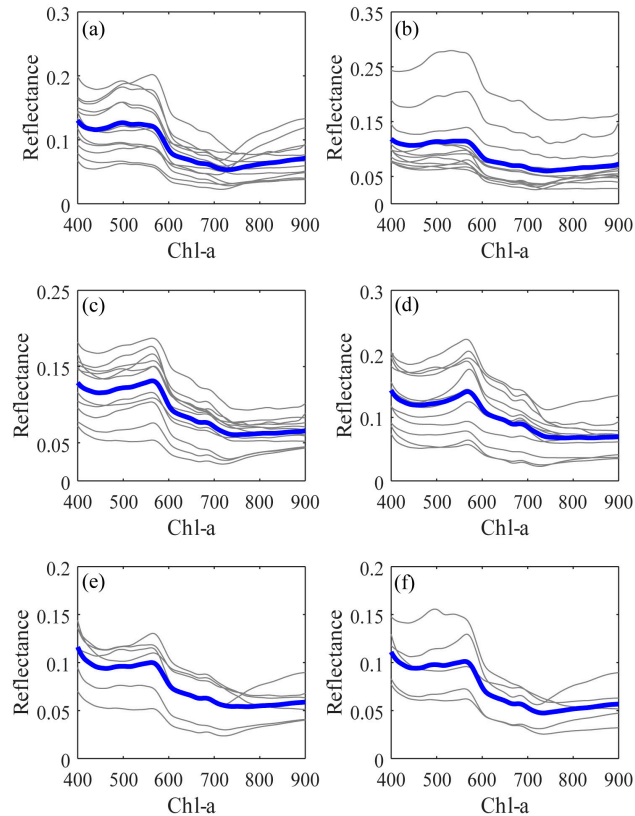


Figure 7. Water-leaving reflectance (R_L) spectra with the spectra average (blue line) for each station ((a–f) are stations 1 to 6 in turn).

We analysed regressions using all possible band ratios in the 400 to 900 nm range and analysed Chl-*a* concentration for each station, as shown in Figure 8. Two-dimensional correlation matrixes indicate the R^2 distribution for all band ratios (250,000 combinations). The yellow regions indicate high R^2 values for calibration between band ratios and Chl-*a* concentration, with most figures indicating that high R^2 values appear in the NIR and red regions (near 680–710 nm) and green region (near 500–600 nm). However, Figure 8a shows no correlation between NIR/red ratio and Chl-*a* concentration, which may indicate that the NIR/red ratio doesn't fit for water areas with lower and narrower Chl-*a* concentration ranges, as indicated the lowest mean and SD values shown in Table 2, which is consistent with a previous study on band ratio analysis [18].

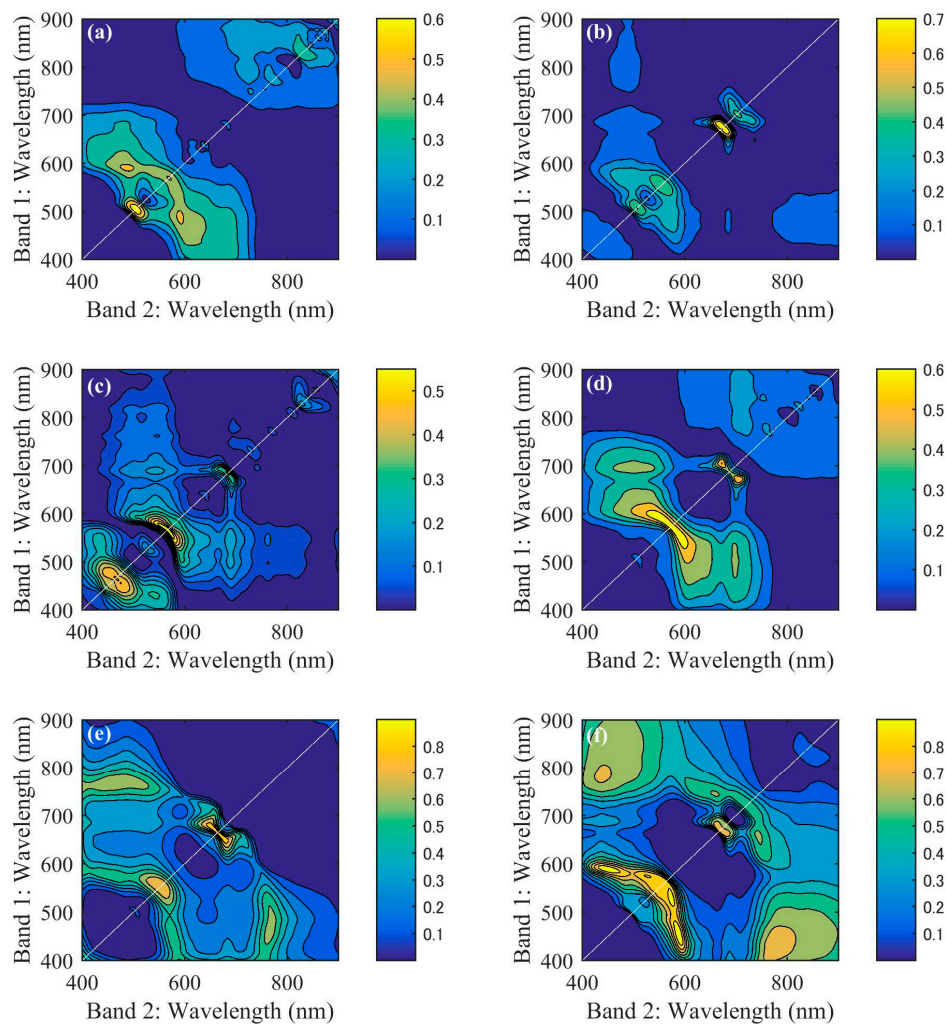


Figure 8. Two-dimensional R^2 distributions obtained through sequential regressions using all band ratios and chlorophyll *a* (Chl-*a*) concentrations for each station ((a–f) are stations 1 to 6 in turn).

We conducted calibrations between the three-band algorithm and Chl-*a* concentration at each station, the results of which are shown in Figure 9. We selected three optimal wavebands using a tuning method before conducting calibration for each station. It is apparent that station 4 performed better than other stations (1, 2, and 3) with the same dataset number ($N = 12$), with a R^2 value of 0.66, using wavebands of 674, 705, and 750 nm. However, we obtained a poor R^2 at station 1, which had the lowest Chl-*a* concentration in this study, using wavebands of 664, 689, and 750 nm. These results may indicate that the three-band algorithm performs well in water with relatively higher Chl-*a* concentrations, which is consistent with several previous studies [19,22]. Figure 9e,f also show better

R^2 values (0.63 at station 5 and 0.81 at station 6) with calibration between the three-band algorithm and Chl-*a* concentration. This provides a possibility of using the three-band algorithm to estimate Chl-*a* in these areas; nevertheless, a shortness of data ($N = 6$ at station 5, $N = 5$ at station 6) may also provide uncertainty to the results.

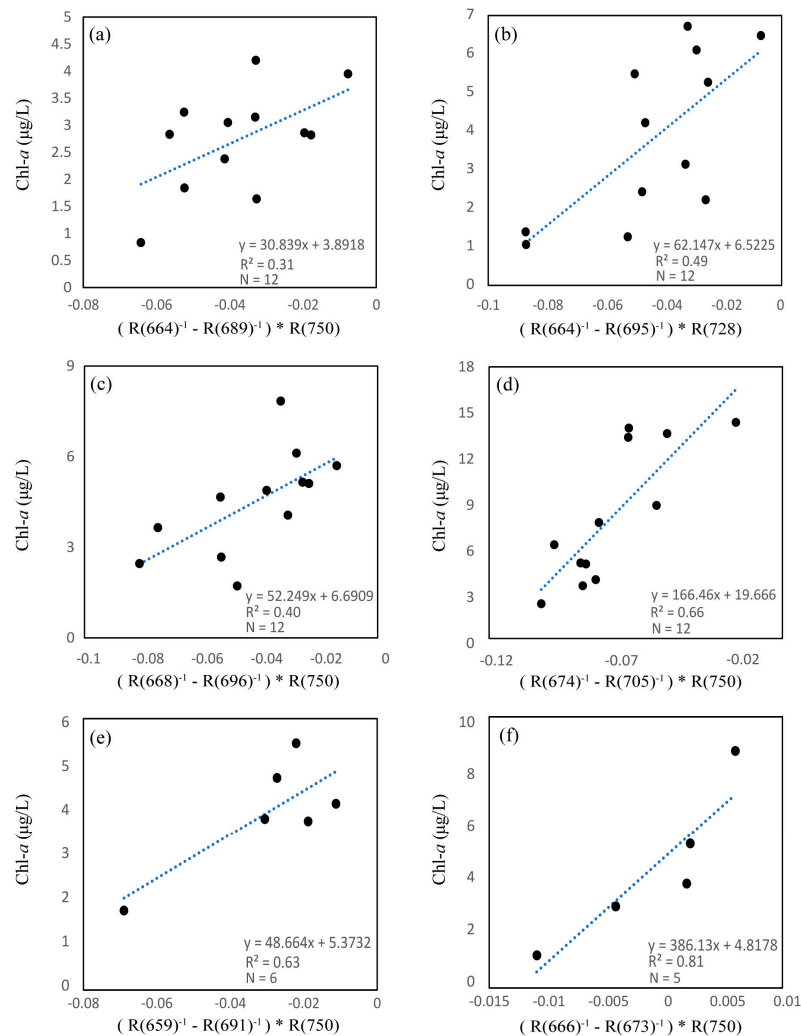


Figure 9. Calibrations between the three-band model algorithm and chlorophyll a (Chl-*a*) concentrations ((a–f) are stations 1 to 6 in turn).

3.3. ISE-PLS Calibration and Validation

ISE-PLS selected optimal variables both for R_L and FDR data due to the iterative stepwise elimination function, to select the optimal NLV in the final model, the relationship between $RMSE_r + J_T$ and NLV (from 1 to 10) were analysed, as shown in Figure 10. The minimum value showed the optimal NLV (6 for R_L and 4 for FDR), larger NLV indicated over-fitting and lower NLV indicated under-fitting. Table 4 summarizes ISE-PLS calibration and validation results using R_L and FDR for Chl-*a* retrieval. As Table 4 shows, ISE-PLS had the same R^2 values (0.83 for both R_L and FDR) and slightly different RMSE values (1.29 for R_L and 1.28 for FDR) for calibration. We also found that ISE-PLS using both datasets had better Chl-*a* retrieval performance than other algorithms, which was indicated by R^2 (0.77 for R_L and 0.78 for FDR) and RPD (2.10 for R_L and 2.13 for FDR) values in the validation results. ISE-PLS using FDR performed marginally better than ISE-PLS using R_L because of the higher R^2 and RPD and lower RMSE (1.47 for R_L and 1.45 for FDR) values for validation. Figure 11a,c show validation

plots for ISE-PLS using R_L and FDR, respectively. Both figures show a close linear relationship between predicted and observed Chl-*a* with the exception of a few scatter points.

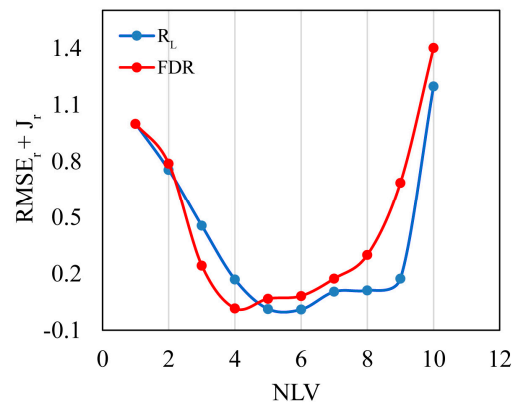


Figure 10. Results for the $RMSE_r + J_r$ when using different number of latent variables (NLV).

Because of the iterative stepwise elimination function, we selected the optimal wavebands using ISE-PLS for both R_L and FDR datasets based on the lowest RMSE for validation, as shown in Figure 11b,d. Selected wavebands for R_L ranged from 495 to 496 nm [43], 589 to 593 nm [44], and 660 to 667 nm [45], which had been proven related to phytoplankton absorption, 544 to 549 nm [43], and 689 to 696 nm [32], which indicated relationship with Chl-*a* fluorescence, and 730 nm which is also sometimes used for Chl-*a* retrieval [45]. We selected a total of 30 (6%) informative wavebands from all 501 wavebands. And for FDR, we selected 10 (2%) informative wavebands from all 501 wavebands.

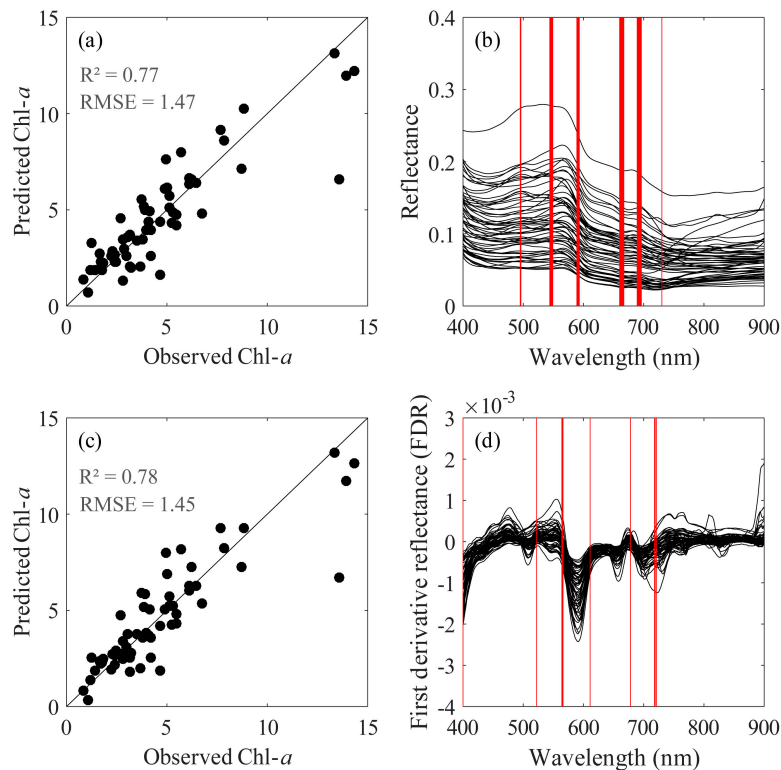


Figure 11. Relationship between observed and predicted chlorophyll *a* (Chl-*a*) (a) water-leaving reflectance (R_L); (c) first derivative reflectance (FDR), and selected wavebands by iterative stepwise elimination partial least squares (ISE-PLS) for Chl-*a* retrieval (b) R_L ; (d) FDR.

Table 4. The coefficient of determination (R^2) and root mean square error (RMSE) for calibration of iterative stepwise elimination partial least squares (ISE-PLS) and leave-one-out (LOO) cross-validation using the entire dataset ($N = 59$), with residual predictive deviation (RPD), number of wavebands, and percent ratio in the full spectrum ($i = 501$).

Dataset	N	Calibration			Validation			Number of Selected Wavebands	Percentage of Selected Wavebands (%)
		NLV	R^2	RMSE	R^2	RMSE	RPD		
R_L	59	6	0.83	1.29	0.77	1.47	2.1	30	6.0
FDR	59	4	0.83	1.28	0.78	1.45	2.13	10	2.0

N, number of samples; NLV, number of latent variables; R_L , water-leaving reflectance; FDR, first derivative reflectance.

In this study, station 4 may have been affected by river nutrients, we carried out ISE-PLS regressions using the R_L dataset except for at station 4 to decrease the impact of different water types. Figure 12 shows the validation plot between observed and predicted Chl-*a*, which was obtained using the LOO method in the ISE-PLS regression. As we can see, the maximum Chl-*a* concentration (from 14.33 to 8.74 $\mu\text{g/L}$) decreased after removing the station 4 dataset. Results shows a close linear relationship between observed and predicted Chl-*a*; however, compared to the R^2 value (0.77) obtained by ISE-PLS validation using all datasets ($N = 59$), a relatively lower R^2 value (0.72) was obtained using the datasets except station 4 ($N = 47$), which may indicate that ISE-PLS performed better in water areas with a wide range of Chl-*a* concentrations.

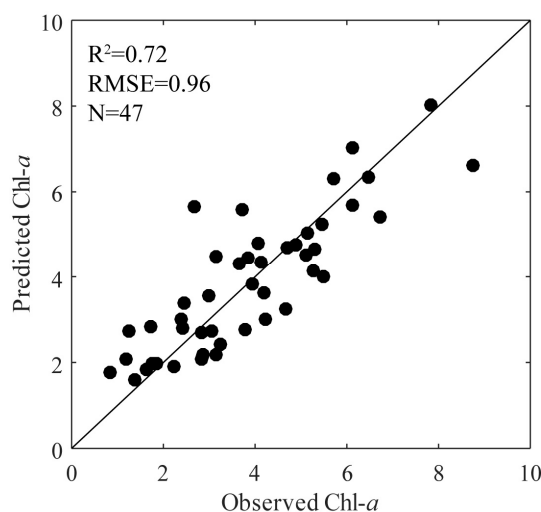


Figure 12. Validation of iterative stepwise elimination partial least squares (ISE-PLS) method using lower chlorophyll *a* (Chl-*a*) concentration dataset (station 4 not included).

4. Discussion

4.1. Empirical and Semi-Analytical Models Performance

In the present study, several empirical and semi-analytical models have been established for Chl-*a* estimation in the Seto Inland Sea. Results show all the standard empirical OC algorithms have underestimated the in situ Chl-*a*, which turns out to be lower RMSE values. The underestimated Chl-*a* calculated from standard satellite algorithms possibly due to the uncertainty in the performance of atmospheric-correction algorithms [46]. The coefficients for OC algorithms have been recalculated using in situ Chl-*a* and hyperspectral dataset, however, OC algorithms using recalculated coefficients also show lower R^2 and higher RMSE values. The three-band model utilized in this study shows a better R^2 than all OC algorithms, and the optimal spectral bands (664, 695, and 736 nm) selected from band tuning are in accord with previous study [19]. However, the low accuracy may indicate the model is unstable as the RMSE shown, which may attribute to the lower Chl-*a* concentration (maximum value

of 14.33 $\mu\text{g/L}$) in this study, because other optically active constituents (CDOM, tripton etc.) may affect the water reflection properties [47]. Similarly, the NIR/red tuning model also shows a better R^2 than OC algorithms, while a poor accuracy, the optimal spectral bands (666 and 693 nm) are in accord with previous study [19]. For the NIR/red model using bands 670 and 705 nm, result shows a poor accuracy, which may attribute to the red shift property [48], that is, there is a red shift in the fluorescence peak to the longer wavelength in higher Chl-*a* concentration waters.

4.2. ISE-PLS Performance

Through the above analyses, it has been shown that ISE-PLS using both R_L and FDR performed better than other algorithms, including the OC, three-band model, and NIR/red two-band model algorithms, indicated by higher R^2 and lower RMSE values. This finding is consistent with previous studies in which PLS method can be used as useful method in retrieval of water quality parameters [22,25]. In addition, ISE-PLS using FDR performed better than ISE-PLS using R_L as indicated by higher R^2 and RPD values and lower RMSE for validation. This may have resulted from derivative analysis reducing random noise and removing the effects of suspended matter on Chl-*a* concentration estimates [22]. Using ISE-PLS, a total of 30 (6%) wavebands for R_L and 10 (2%) wavebands for FDR have been selected as optimal bands from all 501 wavebands, separately, which indicate that 94% wavebands when using R_L and 98% wavebands when using FDR are redundant for Chl-*a* estimation in the Seto Inland Sea. This result provide an evidence that ISE-PLS can be used as an approach for optimal wavebands selection, especially when using hundreds wavebands of hyperspectral data.

4.3. Applications of ISE-PLS Method

This study established a potential model for Chl-*a* estimation in the Seto Inland Sea, which provide the possibility for detecting HABs, since Chl-*a* concentrations can be used as indices of HABs [30]. In general, HABs detection using Chl-*a* algorithms involve the generalized relationship between a high chlorophyll content and HABs occurrences [6]. However, due to the sampling data show lower Chl-*a* concentrations and short of HABs occurrences data, it is difficult to build the relationship between HABs and Chl-*a* concentrations in this study. Nevertheless, the ISE-PLS is a useful method to estimate Chl-*a* concentration, which can be used to evaluate the water quality, so as to management the aquaculture in the Seto Inland Sea.

5. Conclusions

In this study, we developed various models for estimating water Chl-*a* concentration in the Seto Inland Sea, including ISE-PLS using both R_L and FDR and other methods such as OC, three-band model, and two-band model algorithms. Our results showed that the ISE-PLS method is effective for predicting Chl-*a* concentration in the Seto Inland Sea using in situ measured spectral data. With a higher prediction accuracy, ISE-PLS also selects important wavebands that match previously published studies. Additionally, ISE-PLS using FDR is marginally enhanced compared to using R_L for Chl-*a* retrieval. However, OC algorithms are not robust in this present study, and three-band and two-band model algorithms did not perform well in water areas with lower Chl-*a* concentration. Our results also indicate that the ISE-PLS method can perform better when used in water areas with a wide range of Chl-*a* concentrations. These results provide potential insights into coastal water quality assessment by using a Chl-*a* estimation method with hyperspectral measurements.

Author Contributions: Y.S., Z.W. and K.K. designed this study and the fieldwork; Z.W., K.K. and S.O. performed the fieldwork; Z.W. analyzed the data and wrote the manuscript; Z.W. and Y.S. revised the paper.

Funding: This study was supported by the Environmental Research and Technology Development Fund (S9) of the Ministry of the Environment, Japan, and JSPS KAKENHI (16H05631, 17H04625).

Conflicts of Interest: The authors declare no conflict of interests.

References

1. Hashimoto, H.; Hashimoto, T.; Matsuda, O.; Tada, K.; Tamai, K.; Uye, S.; Yamamoto, T. Biological productivity of lower trophic levels of the Seto Inland Sea. In *Sustainable Development in the Seto Inland Sea, Japan—From the View Point of Fisheries*; Okaichi, T., Yanagi, T., Eds.; Terra Scientific Publishing Company: Tokyo, Japan, 1997; pp. 17–58.
2. Yoshie, N.; Guo, X.; Fujii, N.; Komorita, T. Ecosystem and nutrient dynamics in the Seto Inland Sea, Japan. In *Interdisciplinary Studies on Environmental Chemistry—Marine Environmental Modelling and Analysis*; Omori, K., Guo, X., Yoshie, N., Fujii, N., Handoh, I.C., Isobe, A., Tanabe, S., Eds.; Terrapub: Tokyo, Japan, 2011; pp. 39–49.
3. Nishijima, W.; Umehara, A.; Sekito, S.; Okuda, T.; Nakai, S. Spatial and temporal distributions of Secchi depths and chlorophyll a concentrations in the Suo Nada of the Seto Inland Sea, Japan, exposed to anthropogenic nutrient loading. *Sci. Total Environ.* **2016**, *571*, 543–550. [[CrossRef](#)] [[PubMed](#)]
4. Yamamoto, T. The Seto Inland Sea—Eutrophic or oligotrophic. *Mar. Pollut. Bull.* **2003**, *47*, 37–42. [[CrossRef](#)]
5. Imai, I.; Yamaguchi, M.; Hori, Y. Eutrophication and occurrences of harmful algal blooms in the Seto Inland Sea, Japan. *Plankton Benthos Res.* **2006**, *1*, 71–84. [[CrossRef](#)]
6. Yunus, A.P.; Dou, J.; Sravanthi, N. Remote sensing of chlorophyll-a as a measure of red tide in Tokyo Bay using hotspot analysis. *Remote Sens. Appl. Soc. Environ.* **2015**, *2*, 11–25. [[CrossRef](#)]
7. Noh, J.H.; Kim, W.; Son, S.H.; Ahn, J.; Park, Y. Remote quantification of *Cochlodinium polykrikoides* blooms occurring in the East Sea using geostationary ocean color imager (GOCI). *Harmful Algae* **2018**, *73*, 129–137. [[CrossRef](#)] [[PubMed](#)]
8. Zhao, J.; Ghedira, H. Monitoring red tide with satellite imagery and numerical models: A case study in the Arabian Gulf. *Mar. Pollut. Bull.* **2014**, *79*, 305–313. [[CrossRef](#)] [[PubMed](#)]
9. Wang, X.J.; Liu, R.M. Spatial analysis and eutrophication assessment for chlorophyll a in Taihu Lake. *Environ. Monit. Assess.* **2005**, *101*, 1–8.
10. Gholizadeh, M.H.; Melesse, A.M.; Reddi, L. A comprehensive review on water quality parameters estimation using remote sensing techniques. *Sensors* **2016**, *16*, 1298. [[CrossRef](#)] [[PubMed](#)]
11. Katlane, R.; Dupouy, C.; Zargouni, F. Chlorophyll and turbidity concentration as an index of water quality of the Gulf of Gabes from MODIS in 2009. *Teledetection* **2012**, *11*, 263–271.
12. O'Reilly, J.E.; Maritorena, S.; Mitchell, B.G.; Siegel, D.A.; Carder, K.L.; Garver, S.A.; Kahru, M.; McClain, C. Ocean color chlorophyll algorithms for SeaWiFS. *J. Geophys. Res.* **1998**, *103*, 24937–24953. [[CrossRef](#)]
13. O'Reilly, J.E.; Maritorena, S.; O'Brien, M.C.; Siegel, D.A.; Toole, D.; Menzies, D.; Smith, R.C.; Mueller, J.L.; Mitchell, B.G.; Mati, K.; et al. *SeaWiFS Postlaunch Calibration and Validation Analyses, Part 3*; NASA Technical Memorandum 2000-206892; Hooker, S.B., Firestone, E.R., Eds.; NASA Goddard Space Flight Center: Greenbelt, MD, USA, 2000; Volume 11, p. 49.
14. Moses, W.J.; Gitelson, A.A.; Perk, R.L.; Gurlin, D.; Rundquist, D.C.; Leavitt, B.C.; Barrow, T.M.; Brakhage, P. Estimation of chlorophyll-a concentration in turbid productive waters using airborne hyperspectral data. *Water Res.* **2012**, *46*, 993–1004. [[CrossRef](#)] [[PubMed](#)]
15. Gitelson, A.A. The nature of the peak near 700 nm on the radiance spectra and its application for remote estimation of phytoplankton pigments in inland waters. *Opt. Eng. Remote Sens.* **1993**, *1971*, 170–179.
16. Mittenzwey, K.H.; Ullrich, S.; Gitelson, A.A.; Kondratiev, K.Y. Determination of chlorophyll a of inland waters on the basis of spectral reflectance. *Limnol. Oceanogr.* **1992**, *37*, 147–149. [[CrossRef](#)]
17. Sakuno, Y.; Miño, E.R.; Nakai, S.; Mutsuda, H.; Okuda, T.; Nishijima, W.; Castro, R.; García, A.; Peña, R.; Rodríguez, M.; Depratt, G.C. Chlorophyll and suspended sediment mapping to the Caribbean Sea from rivers in the capital city of the Dominican Republic using ALOS AVNIR-2 data. *Environ. Monit. Assess.* **2014**, *186*, 4181–4193. [[CrossRef](#)] [[PubMed](#)]
18. Han, L.; Rundquist, D. Comparison of NIR/RED ratio and first derivative of reflectance in estimating algal-chlorophyll concentration: A case study in a turbid reservoir. *Remote Sens. Environ.* **1997**, *62*, 253–261. [[CrossRef](#)]
19. Dall'Olmo, G.; Gitelson, A.A.; Rundquist, D.C. Towards a unified approach for remote estimation of chlorophyll-a in both terrestrial vegetation and turbid productive waters. *Geophys. Res. Lett.* **2003**, *30*, 1038. [[CrossRef](#)]

20. Wold, H. Estimation of Principal Components and Related Models by Iterative Least Squares. In *Multivariate Analysis*; Krishnaiah, P.R., Ed.; Academic Press: New York, NY, USA, 1996; pp. 391–420.
21. Kawamura, K.; Watanabe, N.; Sakanoue, S.; Inoue, Y. Estimating forage biomass and quality in a mixed sown pasture based on partial least squares regression with waveband selection. *Grassl. Sci.* **2008**, *54*, 131–145. [[CrossRef](#)]
22. Song, K.; Li, L.; Tedesco, L.P.; Li, S.; Duan, H.; Liu, D.; Hall, B.E.; Du, J.; Li, Z.; Shi, K.; et al. Remote estimation of chlorophyll-*a* in turbid inland waters: Three band model versus GA-PLS model. *Remote Sens. Environ.* **2013**, *136*, 342–357. [[CrossRef](#)]
23. Song, K.; Li, L.; Tedesco, L.P.; Li, S.; Clercin, N.; Li, Z.C.; Shi, K. Hyperspectral determination of eutrophication for a water supply source via genetic algorithm-partial least square (GA-PLS) modeling. *Sci. Total Environ.* **2012**, *426*, 220–232. [[CrossRef](#)] [[PubMed](#)]
24. Boggia, R.; Forina, M.; Fossa, P.; Mosti, L. Chemometric study and validation strategies in the structure-activity relationships of new class of cardiotoxic agents. *Quant. Struct. Act. Relatsh.* **1997**, *16*, 201–213. [[CrossRef](#)]
25. Wang, Z.; Kawamura, K.; Sakuno, Y.; Fan, X.; Gong, Z.; Lim, J. Retrieval of chlorophyll-*a* and total suspended solids using iterative stepwise elimination partial least squares (ISE-PLS) regression based on field hyperspectral measurements in irrigation ponds in Higashiroshima, Japan. *Remote Sens.* **2017**, *9*, 264. [[CrossRef](#)]
26. Pawar, V.; Matsuda, O.; Yamamoto, T.; Hashimoto, T.; Rajendran, N. Spatial and temporal variations of sediment quality in and around fish cage farms: A case study of aquaculture in the Seto Inland Sea, Japan. *Fish. Sci.* **2001**, *67*, 619–627. [[CrossRef](#)]
27. Pawar, V.; Matsuda, O.; Fujisaki, N. Relationship between feed input and sediment quality of the fish cage farms. *Fish. Sci.* **2002**, *68*, 894–903. [[CrossRef](#)]
28. Hu, C.; Lee, Z.; Franz, B. Chlorophyll *a* algorithms for oligotrophic oceans: A novel approach based on three-band reflectance difference. *J. Geophys. Res.* **2012**, *117*, C01011. [[CrossRef](#)]
29. Oyama, Y.; Matsushita, B.; Fukushima, T.; Matsushige, K.; Imai, A. Application of spectral decomposition algorithm for mapping water quality in a turbid lake (Lake Kasumigaura Japan) from Landsat TM data. *ISPRS J. Photogramm. Remote Sens.* **2009**, *64*, 73–85. [[CrossRef](#)]
30. Stumpf, R.P. Applications of Satellite Ocean Color Sensors for Monitoring and Predicting Harmful Algal Blooms. *J. Hum. Ecol. Risk Assess.* **2001**, *7*, 1363–1368. [[CrossRef](#)]
31. Tomlinson, M.C.; Stumpf, R.P.; Ransibrahmanakul, V.; Truby, E.W.; Kirkpatrick, G.J.; Pederson, B.A.; Vargo, G.A.; Heil, C.A. Evaluation of the use of SeaWiFS imagery for detecting *Karenia brevis* harmful algal blooms in the eastern Gulf of Mexico. *Remote Sens. Environ.* **2004**, *91*, 293–303. [[CrossRef](#)]
32. Dall’Olmo, G.; Gitelson, A.A. Effect of bio-optical parameter variability on the remote estimation of chlorophyll-*a* concentration in turbid productive waters: Experimental results. *Appl. Opt.* **2006**, *45*, 3577–3592. [[CrossRef](#)] [[PubMed](#)]
33. Gitelson, A.A.; Dall’Olmo, G.; Moses, W.; Rundquist, D.C.; Barrow, T.; Fisher, T.R.; Gurlin, D.; Holz, J.A. Simple semi-analytical model for remote estimation of chlorophyll-*a* in turbid waters: Validation. *Remote Sens. Environ.* **2008**, *112*, 3582–3593. [[CrossRef](#)]
34. Zimba, P.V.; Gitelson, A.A. Remote estimation of chlorophyll concentration in hypereutrophic aquatic systems: Model tuning and accuracy optimization. *Aquaculture* **2006**, *256*, 272–286. [[CrossRef](#)]
35. Gitelson, A.A. The peak near 700 nm on radiance spectra of algae and water: Relationships of its magnitude and position with chlorophyll concentration. *Int. J. Remote Sens.* **1992**, *13*, 3367–3373. [[CrossRef](#)]
36. D’Archivio, A.A.; Maggi, M.A.; Ruggieri, F. Modelling of UPLC behaviour of acylcarnitines by quantitative structure–retention relationships. *J. Pharm. Biomed. Anal.* **2014**, *96*, 224–230. [[CrossRef](#)] [[PubMed](#)]
37. Li, X.L.; He, Y. Chlorophyll assessment and sensitive wavelength exploration for tea (*Camellia sinensis*) based on reflectance spectral characteristics. *HortScience* **2008**, *43*, 1–6.
38. Forina, M.; Casolino, C.; Almansa, E.M. The refinement of PLS models by iterative weighting of predictor variables and objects. *Chemom. Intell. Lab. Syst.* **2003**, *68*, 29–40. [[CrossRef](#)]
39. Williams, P.C. Implementation of Near-Infrared Technology. In *Near-Infrared Technology in the Agricultural and Food Industries*, 2nd ed.; Williams, P.C., Norris, K., Eds.; Association of Cereal Chemists Inc.: Eagan, MN, USA, 2001; pp. 145–169.

40. Chang, C.; Laird, D.A. Near-infrared reflectance spectroscopic analysis of soil C and N. *Soil Sci.* **2002**, *167*, 110–116. [[CrossRef](#)]
41. Gowen, A.A.; Downey, G.; Esquerre, C.; O'Donnell, C.P. Preventing over-fitting in PLS calibration models of near-infrared (NIR) spectroscopy data using regression coefficients. *J. Chemom.* **2011**, *25*, 375–381. [[CrossRef](#)]
42. Yacobi, Y.Z.; Moses, W.J.; Kaganovsky, S.; Sulimani, B.; Leavitt, B.C.; Gitelson, A.A. NIR-red reflectance-based algorithms for chlorophyll-*a* estimation in mesotrophic inland and coastal waters: Lake Kinneret case study. *Water Res.* **2011**, *45*, 2428–2436. [[CrossRef](#)] [[PubMed](#)]
43. Pérez, G.; Queimaliños, C.; Balseiro, E.; Modenutti, B. Phytoplankton absorption spectra along the water column in deep North Patagonian Andean lakes (Argentina). *Limnologica* **2007**, *37*, 3–16. [[CrossRef](#)]
44. Sasaki, H.; Tanaka, A.; Iwataki, M.; Touke, Y.; Siswanto, E.; Tan, C.K.; Ishizaka, J. Optical properties of the red tide in Isahaya Bay, south-western Japan: Influence of chlorophyll *a* concentration. *J. Oceanogr.* **2008**, *64*, 511–523. [[CrossRef](#)]
45. Dall'Olmo, G.; Gitelson, A.A.; Rundquist, D.C.; Leavitt, B.; Barrow, T.; Holz, J.C. Assessing the potential of SeaWiFS and MODIS for estimating chlorophyll concentration in turbid productive waters using red and near-infrared bands. *Remote Sens. Environ.* **2005**, *96*, 176–187. [[CrossRef](#)]
46. Brewin, R.J.W.; Raitsos, D.E.; Dall'Olmo, G.; Zarokanellos, N.; Jackson, T.; Racault, M.F.; Hoteit, I. Regional ocean-colour chlorophyll algorithms for the Red Sea. *Remote Sens. Environ.* **2015**, *165*, 64–85. [[CrossRef](#)]
47. Gitelson, A.A.; Schalles, J.F.; Hladik, C.M. Remote chlorophyll-*a* retrieval in turbid, productive estuaries: Chesapeake bay case study. *Remote Sens. Environ.* **2007**, *109*, 464–472. [[CrossRef](#)]
48. Hu, C.M.; Muller-Karger, F.E.; Taylor, C.J.; Carder, K.L.; Kelble, K.; Johns, E.; Hell, C.A. Red tide detection and tracing using MODIS fluorescence data: A regional example in SW Florida Coastal Waters. *Remote Sens. Environ.* **2005**, *97*, 311–321. [[CrossRef](#)]



© 2018 by the authors. Licensee MDPI, Basel, Switzerland. This article is an open access article distributed under the terms and conditions of the Creative Commons Attribution (CC BY) license (<http://creativecommons.org/licenses/by/4.0/>).